Marine and Petroleum Geology 68 (2015) 718–730

Contents lists available at ScienceDirect

Marine and Petroleum Geology

journal homepage: www.elsevier.com/locate/marpetgeo

Research paper

Ongoing methane discharge at well site 22/4b (North Sea) and discovery of a spiral vortex bubble plume motion

J. Schneider von Deimling[a,*], P. Linke[a], M. Schmidt[a], G. Rehder[b]

[a] GEOMAR Helmholtz Centre for Ocean Research Kiel, Germany
[b] Leibniz Institute for Baltic Sea Research Warnemünde, IOW, Germany

ARTICLE INFO

Article history:
Received 19 December 2013
Received in revised form 24 July 2015
Accepted 27 July 2015

Keywords:
Mega gas blowout 22/4b
North Sea
Methane seepage
Multibeam
Spiral vortex
Turbulence
Trapping
Thermocline
Flare imaging

ABSTRACT

First direct evidence for ongoing gas seepage activity on the abandoned well site 22/4b (Northern North Sea, 57°55′ N, 01°38′ E) and discovery of neighboring seepage activity is provided from observations since 2005. A manned submersible dive in 2006 discovered several extraordinary intense seepage sites within a 60 m wide and 20 m deep crater cut into the flat 96 m deep seafloor. Capture and (isotope) chemical analyses of the gas bubbles near the seafloor revealed in situ concentrations of methane between 88 and 90%Vol. with $\delta^{13}C$–CH_4 values around −74‰ VPDB, indicating a biogenic origin. Bulk methane concentrations throughout the water column were assessed by 120 Niskin water samples showing up to 400.000 nM CH_4 in the crater at depth. In contrast, concentrations above the thermocline were orders of magnitude lower, with a median value of 20 nM. A dye tracer injection into the gas seeps revealed upwelling bubble and water motion with gas plume rise velocities up to ~1 ms^{-1} (determined near the seabed). However, the dissolved dye did not pass the thermocline, but returned down to the seabed. Measurements of direct bubble-mediated atmospheric flux revealed low values of 0.7 ± 0.3 kty^{-1}, much less than current state-of-the-art bubble dissolution models would predict for such a strong and upwelling in situ gas bubble flux at shallow water depths (i.e. ~100 m).

Acoustic multibeam water column imaging data indicate a pronounced 200 m lateral intrusion at the thermocline together with high methane concentration at this layer. A partly downward-orientated bubble plume motion is also visible in the acoustic data with potential short-circuiting in accordance to the dye experiment. This observation could partly explain the observed trapping of most of the released gas below the well-established thermocline in the North Sea. Moreover, 3D analyses of the multibeam water column data reveal that the upwelling plume transforms into a spiral expanding vortex while rising through the water column. Such a spiral vortex motion has never been reported before for marine gas seepage and might represent an important process with strong implication on plume dynamics, dissolution behavior, gas escape to the atmosphere, and is considered very important for respective modeling approaches.

1. Introduction

1.1. Natural and man-made subsea methane release in the North Sea

Natural methane release from the seafloor by seep processes is observed virtually on all continental margins (Judd and Hovland, 2007). Estimates suggest marine seeps may contribute ~10–30 Tg yr^{-1} (Kvenvolden et al., 2001) to global geological methane emissions of 30–45 Tg yr^{-1} (Etiope and Klusman, 2002). However, the significance of marine methane seepage for the total atmospheric methane budget and global warming is still under debate (Ciais et al., 2013).

Methane hosted in interstitial water of marine sediments can enter the water column by diffusive porewater transport, convective fluid flow, or gas bubble release. The latter process is a common phenomenon in the North Sea especially along its central geological graben (Fig. 1), and is subject to research since decades (e.g. Hovland and Sommerville, 1985; Judd et al., 1997; Schroot et al., 2005; Schneider von Deimling et al., 2010, 2011). Methane transported into the water column by bubbles efficiently bypasses the

* Corresponding author. Helmholtz-Zentrum für Ozeanforschung Kiel (GEOMAR), 24148 Kiel, Germany.
E-mail address: jschneider@geomar.de (J. Schneider von Deimling).

http://dx.doi.org/10.1016/j.marpetgeo.2015.07.026

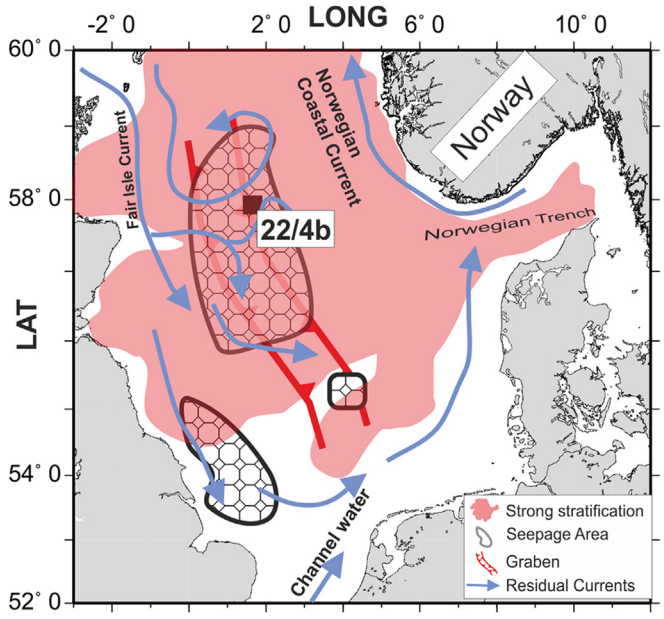

Fig. 1. (a) Schematic main flow pattern in the North Sea adapted from Turrell et al. (1992). Three gas seepage regions (purple polygons) surrounding the study area 22/4b were compiled from various sources (Judd et al., 1997; Judd, 2001; Schroot et al., 2005). Shaded polygon with orange border shows the spatial extent of strong stratification (ΔT 6K) between surface and bottom water in the North Sea modeled for June–August after Holt and Umlauf (2008). (For interpretation of the references to color in this figure legend, the reader is referred to the web version of this article.).

Fig. 2. 22/4b blowout image 1990. Inset shows blowout location. © MOBIL North Sea Ltd. Rig is approximately 60 by 80 m wide.

microbial filter of the shallow seabed (e.g. Sommer et al., 2006). Those bubbles subsequently undergo dissolution during transport through the water column due to under saturation of methane in the surrounding seawater.

Anthropogenic sources for methane gas release from the seabed include pipeline and well leakages, which might be of considerable magnitude if the number of potential leakages in an area of intense hydrocarbon exploration (i.e. North Sea) are taken into account (Vielstaedte et al., in this issue). Judd and Hovland (2007) compiled a series of explosive offshore accidents beginning in 1964 for the North Sea; our study will concentrate on such a blowout that happened at the 22/4b well site in 1990 in the Northern North Sea. In this study, we deliver direct evidence of ongoing gas discharge at site 22/4b since 2005 and provide a comprehensive geochemical and hydroacoustic dataset about this exceptional site.

1.2. History of the well 22/4b blowout and related scientific research

In May 1994, Rehder et al. (1998) identified a pronounced dissolved methane peak in surface waters near 58°N and 1°40′E, about 200 km east off the Scottish coast, with maximum concentrations more than 700 times atmospheric equilibrium. The area was marked in nautical charts as a gas release hazard to marine vessels. Three years before, on the 20th of November 1990, Mobil North Sea Ltd. (MNSL) encountered shallow gas at 360 m below seabed while drilling into the Quaternary section of exploration well UK22/4b. The well blew out, creating a crater on the seafloor and a massive bubble plume (Fig. 2) that rapidly diminished over several days. From 1990 on, this crater and the vigor of the gas plume were monitored by survey vessels and ROV (remotely operated vehicle) operations, showing decreasing plume intensity (Fox, 1995). In 2000, the UK Dept. of Trade and Industry (DTI) determined that further monitoring was not required without a perceived safety threat or environmental harm, and a near future depletion of the gas reservoir was predicted. However, fifteen years after the accident a revisit with R/V ALKOR in 2005 verified a persisting major methane anomaly at the sea surface and provided direct visual and acoustic evidence of a ca. 25 m diameter bubble plume arising from a 60 m wide conical crater at the seabed up to the sea surface (Schneider von Deimling et al., 2007). After a submersible dive in 2006, a press release raised public awareness and political interest for the still continuing massive methane discharge 16 years after the blowout incident. In light of enhanced sensitivity to offshore oil and gas leakage in the wake of the Deep Water Horizon blowout (Gulf of Mexico, 2010), a comprehensive survey with further measuring, monitoring and verification studies at the 22/4b location outlined in Leifer and Judd (in this issue) was initiated by the U.K Department of Energy and Climate Change (DECC).

1.3. Minor vs. major gas plume release

Marine gas seeps can be classified by their flux rate into minor (mL min^{-1}), major (L min^{-1}) (Leifer and Boles, 2005), and mega (10^6 L day^{-1}) release sites (Leifer, in this issue). Minor seeps are characterized by Gaussian-shaped bubble size spectra peaking around 2–3 mm radii with potential spectra variation depending on gas flux magnitude (Leifer, 2010). Major seeps produce broader bubble size spectra characterized by a power law decrease of probability with bubble radius (Leifer, 2010). Modeling suggests that a clean 3 mm radius bubble of methane would loose 95% of its initial amount of methane during a 100 m rise by dissolution into the water column, while absorbing nitrogen and oxygen during the initial part of its rise (Leifer and Patro, 2002). E.g. Schneider von Deimling et al. (2011) demonstrate for a seep site in the Central North Sea at 70 m water depth by modeling and field data that the release of small bubbles has a very limited vertical transport potential. In turn, larger bubbles released from major seeps are far more efficient in regard to vertical gas transport due to their greater volume to surface area ratio and higher rise velocities (e.g. Leifer et al., in this issue). Leifer and Patro (2002) showed that larger bubbles ($r > 5000\ \mu$m) released at about 100 m water depth should transport more than 50% of their original CH_4 content into the atmosphere.

Each rising bubble applies drag to the ambient water, inducing a vertical momentum plume (Milgram, 1983). If sufficiently high, the total momentum can induce significant upwelling with 0.3–2 m/s (Leifer et al., 2009), lifting e.g. denser ambient water and even particles upwards. Bubble rise and related methane gas dissolution/equilibration within an upwelling flow causes an enhanced vertical transport due to reduced bubble retention time in

seawater. Therefore, upwelling is considered so far to foster vertical methane transport (Leifer et al., 2006, 2009; Clark et al., 2010). In case of mega seeps, such as the 22/4b blowout, an interesting question is whether enhanced vertical transport efficiency, that has been observed at major seeps, further scales up with increases in flux.

1.4. Fate of the released methane in the North Sea

Mid-to high-latitude areas like the North Sea are characterized by summerly thermoclines hampering diapycnal mixing between cold, dense water at depth, and warm, light surface water above (Holt and Umlauf, 2008; Nauw et al., in this issue). Schneider von Deimling et al. (2011) suggest trapping of seepage methane in the Central and Northern North Sea underneath the thermocline resulting in low atmospheric flux in summer, and predict enhanced atmospheric CH_4 input from depth with the onset of stratification breakdown in late fall and during winter time. Methane dissolved above the thermocline is considered to be quantitatively transferred to the atmosphere due to air–sea exchange caused by high wind speeds in the North Sea even during summer (WASA, 1998). While the strong thermocline in the Central and Northern North Sea presents a barrier for diapycnal mixing and dissolved gas exchange, seep gas bubble transport across the thermocline is unaffected (Schneider von Deimling et al., 2011).

In situ gas bubble release at our study site 22/4b has been characterized as a mega gas bubble seep site with 90 L s^{-1} at in situ pressure, which represents the strongest methane seep flux quantified to date (Leifer, in this issue). Respective state-of-the-art modeling of the vertical transport of 90 L s^{-1} methane by bubbles including upwelling effects predict high methane fluxes into the upper layer and atmosphere (Leifer et al., in this issue). However, a substantial mismatch between model results and independent field assessments of fluxes at well 22/4b, presented in this issue (this study, Gerilowski et al., Sommer et al., in this issue), point towards possible unknown processes where vertical methane transport through gas bubbles is suppressed.

1.5. Scope of the paper

The present paper provides a comprehensive description of observations at the well site 22/4b, including morphology of the crater, gas bubble release characteristics, geochemical gas source, and dissolved methane distribution to characterize the 22/4b seepage behavior. A discussion on several observations over the years since 2005 allows venturing into qualitative assessments of changes in seep intensity and bottom expression. Finally, modern multibeam acoustic imaging data of the water column is analyzed in detail to identify gas bubble plume related processes, which help elucidating the mismatch between modeling (Leifer et al., in this issue) and field observation of a small methane fraction crossing the thermocline.

2. Instrumentation, methods, and sampling

Most of the relevant data presented here were acquired during the AL290 cruise (R/V ALKOR, Oct.–Nov., 2006) and M82-0 cruise (R/V METEOR, June 2010). Supporting data originate from cruise AL259 (2005), and cruise CE12010 (R/V CELTIC EXPLORER, 2012).

2.1. Continuous sea surface methane measurements

Sea surface methane concentrations were determined in June 2005 (AL259) by using a continuously operating bubble-type/laminar flow air–water equilibration system linked to a gas chromatographic system (Rehder and Suess, 2001). A sequence of 12 measurements, which include measurements of two different calibration gases (approx. 2 ppm V and 10 ppm V in synthetic air, Deuste Steiniger AG, fine calibrated in the Lab of Environmental Physics, Heidelberg), three ambient air measurements, and seven surface water measurements were analyzed every 2 h. The sequence was slightly modified in areas of potentially high air/seawater methane gradients by manually injecting a 1 ml gas sample from the extracted gas phase of the equilibration system directly into the GC. This allowed methane concentration measurement intervals of about 5 min with a precision of approx. 2%.

2.2. Manned submersible and ROV operations

The research submersible JAGO (http://www.geomar.de/en/centre/central-facilities/tlz/jago/) and the ROV KIEL 6000 (http://www.geomar.de/en/centre/central-facilities/tlz/rovkiel6000/) were used for extensive video documentation, gas and plume water sampling in and around the crater, and for fluorescent dye injection to track water motion out of the crater.

The research submersible JAGO, certified to a maximum operating depth of 400 m, can accommodate two persons, the pilot and a scientist/observer. The vehicle is equipped with Fluxgate compass, USBL navigation and tracking system, underwater telephone, horizontal and vertical scanning sonar, video and still cameras inside the submersible, storage CTD (Falmouth Scientific instruments), and an eight function manipulator arm for handling various sampling devices. Unfortunately, USBL navigation was not available during cruise AL290. For dye release experiments, a latex bag filled with 300 g of the colorant “uranin”, dissolved in 2 L of seawater sampled from the planned release depth prior to the experiments, was attached to JAGO within reach of its manipulator arm.

The work-class ROV KIEL 6000 is a 6000 m rated deep diving platform (Schilling Robotics LLC, Davis, USA). For underwater navigation, the ship-based Sonardyne system worked in conjunction with an autonomous transponder mounted on the light rack of the ROV. High-resolution video was recorded with an HD-SDI camera (Kongsberg OE14-500) and by 2 SD cameras (Kongsberg OE14-366 MKII) mounted on pan/tilt units. Three 2 L Niskin water sampling bottles were attached to the ROV frame for sampling of dissolved gases. A modified 62.5 ml stainless steel container equipped with a 1’ pressure-rated ball valve was used for high pressure gas bubble sampling according to Pape et al. (2010).

2.3. Free gas and dissolved gas sampling in the water column

A Seabird 911plus conductivity/temperature/depth (CTD) profiler equipped with twelve 10 L Niskin bottles was used for water column sampling during AL290 cruise. Dissolved methane was vacuum-extracted from water samples (Rehder et al., 1999). As a result, seawater transferred from Niskin bottles into pre-evacuated 2200 ml glass bottles spontaneously degassed. The residual gas phase was recompressed to atmospheric pressure, and a 1 ml gas aliquot was injected into an onboard gas chromatograph equipped with FID. The methane content was calculated according to Keir et al. (2009). The overall accuracy assessment of the analytical method is ±5% based on replicate sample analysis. The remaining gas was stored for further shore-based gas analysis into pre-evacuated crimp-top glass vials containing 2 ml of supersaturated salt solution for contamination-free storage. Selected samples were measured for the stable carbon isotopic signature of methane ($\delta^{13}C–CH_4$) using a continuous flow ir-GC-MS as described by Schmale et al. (2010). $\delta^{13}C–CH_4$ values are reported vs Vienna Pee Dee Belemnite (VPDB) with an overall precision $> \pm 1‰$.

2.4. Water column imaging and seafloor characterization by active acoustics

A hull-mounted KONGSBERG Simrad EK60 single split beam echosounder at 38 kHz was operated aboard R/V ALKOR in 2006 for water column acoustic imaging. 2 kW transmission power via a 1 ms pulse was set and the ping rate adjusted to avoid seafloor multiple echoes in the records. Acoustic absorption was tuned by referring to a salinity value of 35‰. The echosounding system has an opening 3 dB half-power beam angle of 7° and 6.5° and was calibrated 6 months before the survey start with a copper sphere. Volume backscattering strength values Sv were taken from the software ECHOVIEW. No motion compensation was applied to the EK60 data.

Aboard R/V METEOR, several survey lines were run in 2010 at the 22/4b site using the modern broadband KONGSBERG EM710 multibeam echosounder for both, mapping the seabed and investigating the water column in 3D with a 140° opening angle, traveling at a speed of 2 knots. The 1°× 1° hull-mounted EM710 Mills-Cross array was operated with a continuous wave modulated pulse with a 73–98 kHz frequency span for better transmit/receive sector separation performance. The transmit beams were electronically stabilized for pitch and yaw, and the receive beams were stabilized for roll. The target strength of this system was not calibrated, therefore multibeam backscatter investigations presented in this study represent relative values only. Water sound speed profiles were generated by a Valeport sound velocity probe. Generally, the vessel was operated in a "silent mode" to optimize signal to noise ratio vital for water column gas bubble detection. The datasets were post-processed with MBSystem (Caress and Chayes, 2008; release 5.3) and the QPS-Fledermaus software package including FMMidwater (version 7.2). To obtain a useful bathymetric chart of the crater, a ping-by-ping analyses and 3D inspection with manual editing was necessary to reject bad soundings caused from scattering within the water column (e.g. gas bubbles).

The full three dimensional extent of the gas bubble plume scatter was extracted by setting a threshold filter (−20 to −26.5 dB). Precise georeferencing of bubble locations was achieved by raytracing travel-time-angle-amplitude data of each beam with respect to the vertical sound velocity profile. Those georeferenced soundings are presented in a 3D point cloud for spatial analyses and interpretation (Fig. 10). For better visualization of spatiotemporal changes of filtered backscattering strength, the point cloud was interpolated with a 3D near neighbor interpolation run in MATLAB (R2013a) to generate a 3D cube (Supplemental S6, S7, S8 and S9).

Supplementary video related to this article can be found at http://dx.doi.org/10.1016/j.marpetgeo.2015.07.026.

3. Results

3.1. Surface methane concentration survey and surface bubble flux

Concentrations of sea surface methane sampled during AL259 in June 2005 display the same trends as presented by Rehder et al. (1998). Methane concentrations in the Central North Sea were slightly above atmospheric equilibrium (2.73 nM in June 2005; Schneider von Deimling et al., 2011) with the bulk of the data between 2.8 and 3.7 nM. Higher surface concentrations were recorded in the Kattegat region, close to the coast in the Skagerrak, at the Dogger Bank, and when approaching the Elbe River (Fig. 3). Concentrations slightly above 15 nM were encountered in an area close to the blowout site between 57°48′N and 58°18′N, 1°6′–1°45′E. Concentrations close to 100 nM are clustered in two patches, one at the blowout site, and the other one at about 58°7′N, 1°13′E (16.7 km NW of well 22/4b), with a maximum methane concentration of 113 nM. Despite methane concentrations

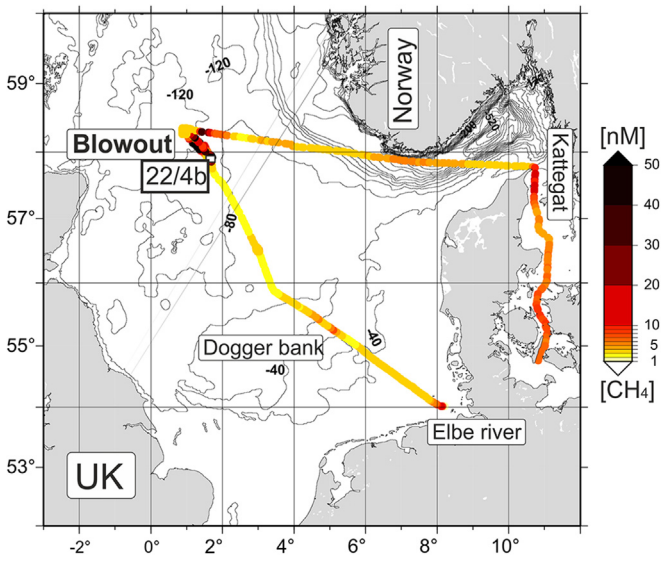

Fig. 3. Surface methane concentration measurements from June 2005 (AL 259) recorded using an equilibrator system with highest concentrations of 113 nM close to 22/4b (note this value is above the color bar range). (For interpretation of the references to color in this figure legend, the reader is referred to the web version of this article.).

an order of magnitude lower, and a smaller area of influence compared to the observations made in 1994 (Rehder et al., 1998), measured data suggest that the blowout site remained a dominant methane source in the open Central and Northern North Sea in 2005.

Bubbles entering the atmosphere (Fig. 5a) were captured at 0.5 m water depth with an inverted funnel during a ZODIAC survey and analyzed with 25% mole fraction CH_4 (Table 1). An upper estimate of the gas bubble surface flux is presented by the following calculation based on our observations in October 2006. Bubble burst events at the sea surface were counted from video analyses to assess the flux rate per second for a count of 500 bubbles per m^2. An average bubble diameter of 1 cm (Fig. 5a) was optically determined with 25 Vol% of methane based on our measurements (Table 1). Multiplication by the bubble plume surface area of 25 m (estimated from the observation deck of R/V ALKOR), encircling areas of homogeneous bubble flux intensities, yields an integrated atmospheric bubble surface CH_4 flux of 32 ± 12 L s^{-1} corresponding to a best estimate of 0.7 ± 0.3 kt y^{-1} (calculated after the ideal gas law at atmospheric pressure).

3.2. Manned submersible and ROV investigations

3.2.1. Visual observations on crater morphology

In 2006, 16 years after the drilling hazard, the first of the two JAGO dives started with a transect from SE towards the crater covering approximately 100 m distance. NW coarsening sediment with shell debris and stones of approximately 20 cm size colonized by sea anemones was observed (Fig. 4a). Inside the crater rim, a dense layer of empty clam shells (*Arctica islandica*) was observed in approx. 20 cm sediment depth (Fig. 4b). The rim itself was colonized with suspension feeders, which benefit from the higher currents at this exposed habitat (Fig. 4c). On the way into the crater, a large number of coalfish (*Pollachius virens*) surrounded and followed the submersible. Occasionally, we observed some individual species of cod (*Gadus morhua*) and haddock (*Melanogrammus aeglefinus*) attracted by the bubbles (and the submersible). Inside the crater, a small terrace became visible (Fig. 4c), whereas the deeper part of the crater below 110 m water depth was formed by steep, almost

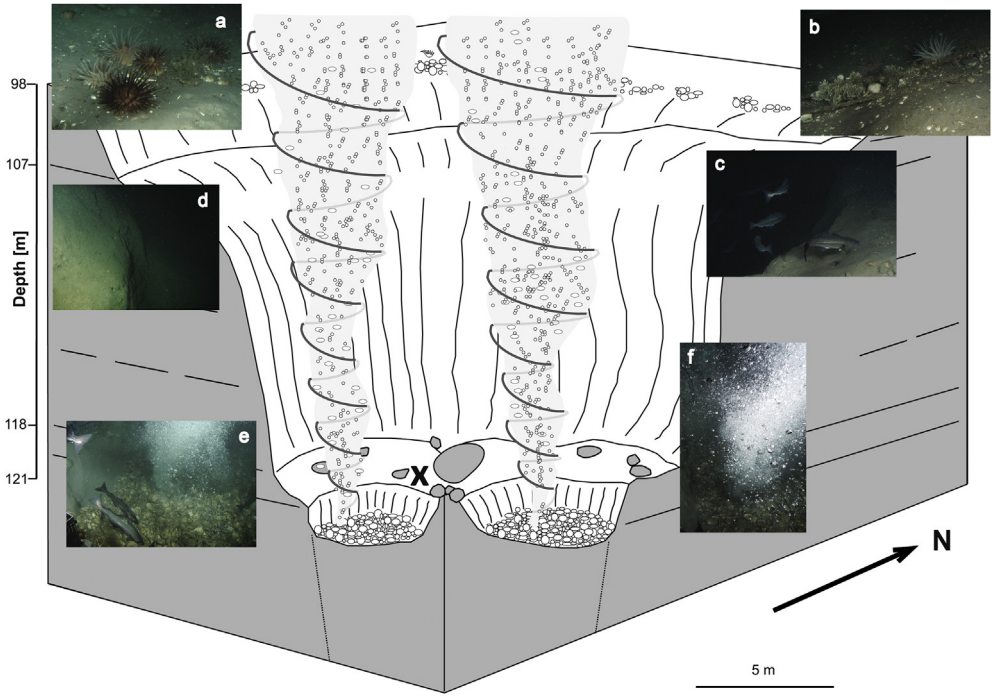

Fig. 4. Schematic drawing of the very first 22/4b crater investigation during the 2006 dives with embedded pictures taken from JAGO illustrating: the crater rim with coarser material (a). colonized by suspension feeders (b), funnel-shaped crater wall with a small terrace (c), steep and eroded crater walls (d), and two out of three major bubble plumes rising from two small basins covered by clam shells at the bottom of the crater (e, f). Water and gas sampling as well as the dye release experiment were conducted from a position on the left hand side of the big bolder on the small ridge between the basins, where intermediate and smaller gas vents emerged (marked by "X").

vertical flanks of prominent sediments with erosive scars (Fig. 4d) generated by vigorous gas and water flow emerging from the center of the crater (Fig. 4e and f). The base of the crater at 120.6 m water depth was divided by a small ridge into two sub-basins, each approx. 5 m in diameter and 1 m in depth (Fig. 4). The bottoms of both basins were covered with large empty shells of *A. islandic*a (Fig. 4e) and there was no evidence of any soft sediment within the crater. At the edges of the basins some minor gas streams were visible, where small patches of sulfide-oxidizing bacteria colonized. In the other areas, no signs of chemo-autotrophic fauna were visible. Compared to these visual observations in 2006, the situation in 2012 was different with sediments covering the clam shells and the two basins at the base of the crater (Supplemental S10).

3.2.2. Visual observations of bubble plume behavior

Visual investigation with JAGO revealed that the gas discharge mainly originated from the center of the crater (Fig. 4). During the observation dives, an inflow current directed towards the center of the crater consistently dragged the submersible into the gas plume. Descending the funnel-shaped crater wall (inclination 40–60°, Fig. 4c), at 112 m water depth, the crater wall appeared vertical, showing signs of erosion and vertical scarps (Fig. 4d). Here, the main bubble plume is visible and video data indicates some spiral rotation of the 4–6 m diameter plume (Supplemental S1). This plume lifted the submersible from 110 m to 72 m water depth within 4 min (15 cm s^{-1}). JAGO finally landed in the center of the crater, at 120.6 m water depth, where three major gas vents approximately 50 cm in diameter with opaque appearance (Fig. 4e and f) and suspended sediment particles in the water column were found. Additionally, many minor gas seeps were identified at the bottom of the crater. The motions of the bubbles were analyzed in more detail for plume uplift and rotary motions while the submersible sat on the seabed (Fig. 5c and d; Supplemental S2). Slow motion video replay revealed that bubbles in the strongest opaque gas jets were released under high pressure with approx. 1 m s^{-1} higher rise velocities compared to bubbles emanating from minor vents. Within the opaque bubble plume some spheroidal clusters of several centimeters to decimeters in diameter occasionally emerged, outpacing the bulk gas jet. Some of the large and clustered bubbles fragmented into smaller individuals after a very short travel time of approximately 1 s. The interface between the gas bubble plume and the ambient water is characterized by unsteady motion with large structural unconformities on a meter scale. The motion of the plume's visible surface is characterized by helical flow (Supplemental S2). The estimated frequency of rotation 1 m above the vent was 2–4 Hz, which is higher than observed 11 m above the vent.

ROV KIEL 6000 observations in 2012 indicate reduced major plume gas releases compared to 2006. However, a new major plume was discovered venting from a jagged scar in the crater wall at 118 m water depth (Fig. 5f). The bubble release intensity appeared at the same order of magnitude as one of three major plumes observed in 2006 and gas release was again characterized by broad bubble size spectra, rotary motion, and strong turbulence (Supplemental S3).

Supplementary video related to this article can be found at http://dx.doi.org/10.1016/j.marpetgeo.2015.07.026.

3.2.3. In situ bubble capturing and dye injection experiment

Gas bubbles captured within the 22/4b crater and from the new crater discovered 2.2 km southeast of 22/4b in 2011 (Leifer, in this issue) mainly contain methane (85–90% Vol.) and some minor components like nitrogen (5–7%), and oxygen (1–2%). Traces (<1 ppm) of higher hydrocarbons (C_2–C_6) also were determined in the gas samples. The measured CO_2-concentrations ranged between 250 and 400 ppm (Table 1). No hydrogen sulfide could be detected in the gas phase. Stable carbon isotope analyses of

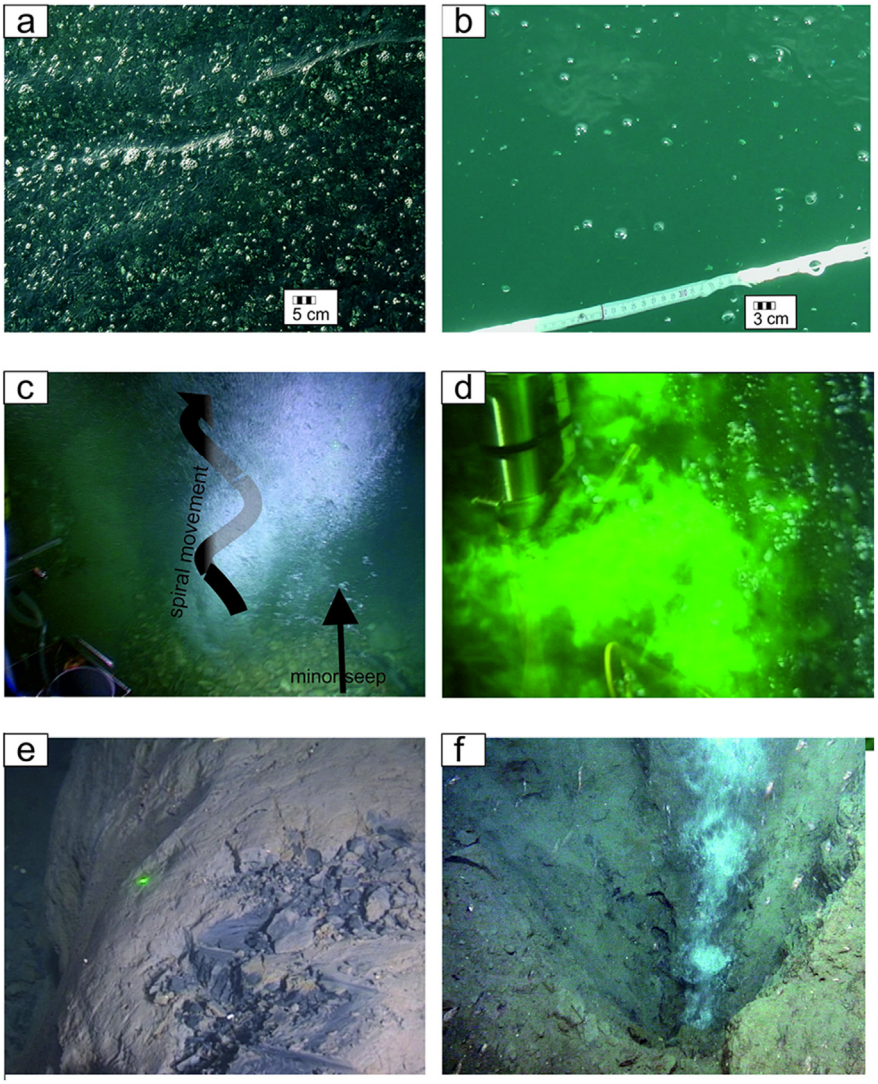

Fig. 5. Pictures showing (a) the bubble plume at the sea surface in 2006 and (b) in 2012, (c) minor seep bubbles in front of the spiral opaque mega plume (Supplemental S2 showing rotation), (d) the uranin dye tracer release within the mega plume showing vertical upwelling, (e) the almost vertical wall of the crater, and (f) a new major/mega seep found in the crater wall in 2012 with a small scale spiral vortex (Supplemental S3).

methane derived from gas bubble samples revealed δ^{13}C-values of about −75‰ VPDB (Table 1; Supplemental S5).

The dye injected into the major gas plume during the 2006 JAGO operations was immediately taken up by a rising momentum plume and subsequently disappeared from JAGO's field of view (Fig. 5d). The sea surface was continuously observed from the top deck of R/V ALKOR during calm sea and good visibility. However, no dye could be seen at the sea surface within 8 min after the dye was injected at the seafloor. Instead, the dye re-emerged at the crater bottom near JAGO's station 2 min and 11 s after the release.

3.3. Nearfield dissolved methane concentrations

Dissolved methane concentrations determined in Niskin samples taken by the submersible JAGO within the blowout crater showed highest concentrations of 400.000 nM (Fig. 6a). A CTD cast into the center of the crater showed highly elevated concentrations around 20,000–60,000 nM in Niskin samples triggered below the thermocline (Fig. 6a). Seawater from 0.5 m water depth sampled from the ZODIAC boat within the surface plume (but without capturing gas bubbles in the Niskin) revealed only 157 nM (Fig. 6a).

3.4. Farfield dissolved methane plume sampling

The hydrographic setting of the water column during the October 2006 survey dates was characterized by a strong thermocline, causing a potential density difference shift of 0.75 kg^{-3} from 38 to 55 m water depth (Fig. 6b) with temperature and salinity values of 12.7°C/35.2 and 9.5°C/35.3, respectively. Advection in the North Sea is controlled by the M2 tide (Otto et al., 1990; Nauw et al., in this issue) and may cause omnidirectional dispersion by tidal mixing of dissolved constituents such as methane over time, depending on meteorological and tidal situation (see model results in Hainbucher et al., 1987; Rehder et al., 1998; Nauw et al., in this issue).

In addition to the CTD cast in the crater (see 3.3), 96 methane measurements from 8 CTD/Rosette water sampling casts were performed nearby the crater and up to 180 m away. One CTD cast, 5.6 km north of 22/4b served as reference station to assess the local hydrography and local dissolved methane concentration background (Fig. 6a). The reference sample site selection was guided by EK60 sonar monitoring of the water column to avoid Niskin bottle gas bubble capture.

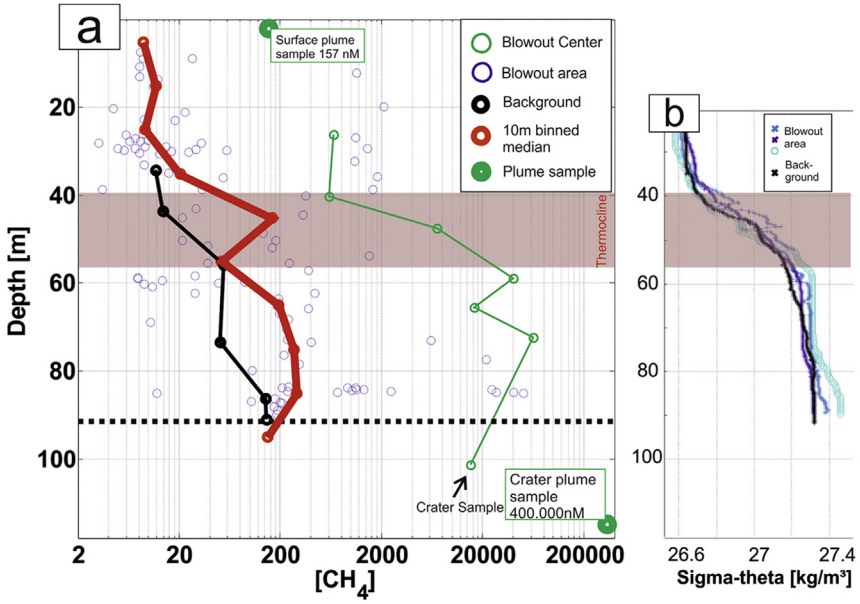

Fig. 6. (a) Methane concentration profiles from 9 CTD casts conducted in the vicinity of (0–180 m; blue dots), at (green), and 5.6 km away (black) from the 22/4b crater center, respectively. Median values were calculated for 10 m bin depth intervals (red). Green dots show values sampled within the upwelling plume in the crater and at the sea surface, respectively. Note logarithmic x-scale methane concentration in nM. (b) CTD density profiles gathered in the vicinity of and 5.6 km away from the 22/4b site. (For interpretation of the references to color in this figure legend, the reader is referred to the web version of this article.)

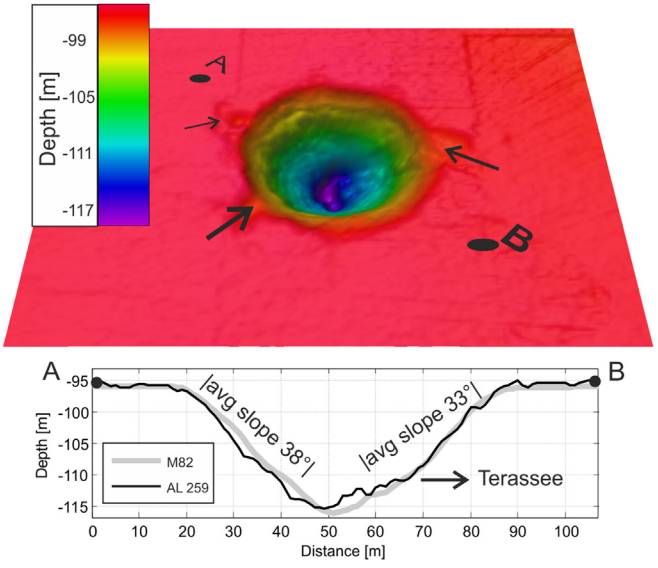

Fig. 7. 1.5 m gridded bathymetry (cruise M82, 2010) of the 22/4b crater, illumination from northwest. Depth profile is taken from A (NW) across the crater to B (SE). Rim scars are indicated by arrows. Profile additionally includes AL 259 data from 2005 (Schneider von Deimling et al., 2007).

The vertical density profiles recorded by the CTD in the vicinity of and 5.6 km away from well site 22/4b are basically identical (Fig. 6b). The minimum methane concentration of 3.2 nM at 28 m water depth falls within the range of background concentrations of inflowing waters from the North Atlantic (Rehder et al., 1998) and reported background data for the Central North Sea (Schneider von Deimling et al., 2011).

To better constrain the vertical methane distribution, concentration data from all stations except the reference station were binned into 10 m intervals and the median methane concentration in each hydrographic layer was calculated (Fig. 6a, red circles). The bulk methane concentration profile shows a general trend with concentrations one to two orders of magnitude higher at depth compared to the surface layer. The steepest gradient in the median methane concentration profile occurs within the thermocline, with a distinct decrease between 50 and 40 m (200 nM) and 40–30 m (20 nM) water depth.

Background methane values gathered 5.6 km (3 nmi) north of the blowout site generally show a similar trend, but with much lower methane values.

3.5. Crater bathymetry and acoustic water column imaging of gas plumes

A comparison between bathymetry from Schneider von Deimling et al. (2007) and bathymetric data gathered in 2010 reveals only minor differences (Fig. 7). The 2010 dataset shows three 1 m deep scars on the rim of the crater pointing towards the center. The average slope between the top rim towards the crater center is 35° with a peak in the lower third of the crater wall with 56° (Fig. 7). Gradients of the crater wall bathymetry occasionally mismatch visual observations, the latter showing an almost vertical crater wall at some locations (e.g. Fig. 5e). Those differences may arise from measurements with different beam angles and bottom detection algorithms of the respective multibeam systems and data gridding limitations with smoothing effects for extreme morphologies such as crater walls. The maximum acoustic sounding depth was determined at 118.6 m, which roughly agrees with the 120.6 m JAGO pressure measurement at the center of the crater.

Water column analyses with single beam echosounder measurements in the blowout area in 2006 (Fig. 8a) reveal elevated acoustic backscatter vertically extending from the seafloor up to the hull-mounted transducer at about 4 mbsl (Fig. 8b). The high volume backscattering pattern achieves horizontal extents of 20 m. To the left, the acoustic bubble plume is enclosed by a weaker and narrower enhanced backscattering, (blue) slightly above the noise level of ~ -80 *dB* re 1 μPa being aligned parallel to the high intensities. Wavy patterns emerge e.g. on the left side of the acoustic plume in Fig. 8b on a meter to tens of meters scale. 50 m to the right of the main plume, a second vertical feature with high backscattering appears between 10 and 50 mbsl

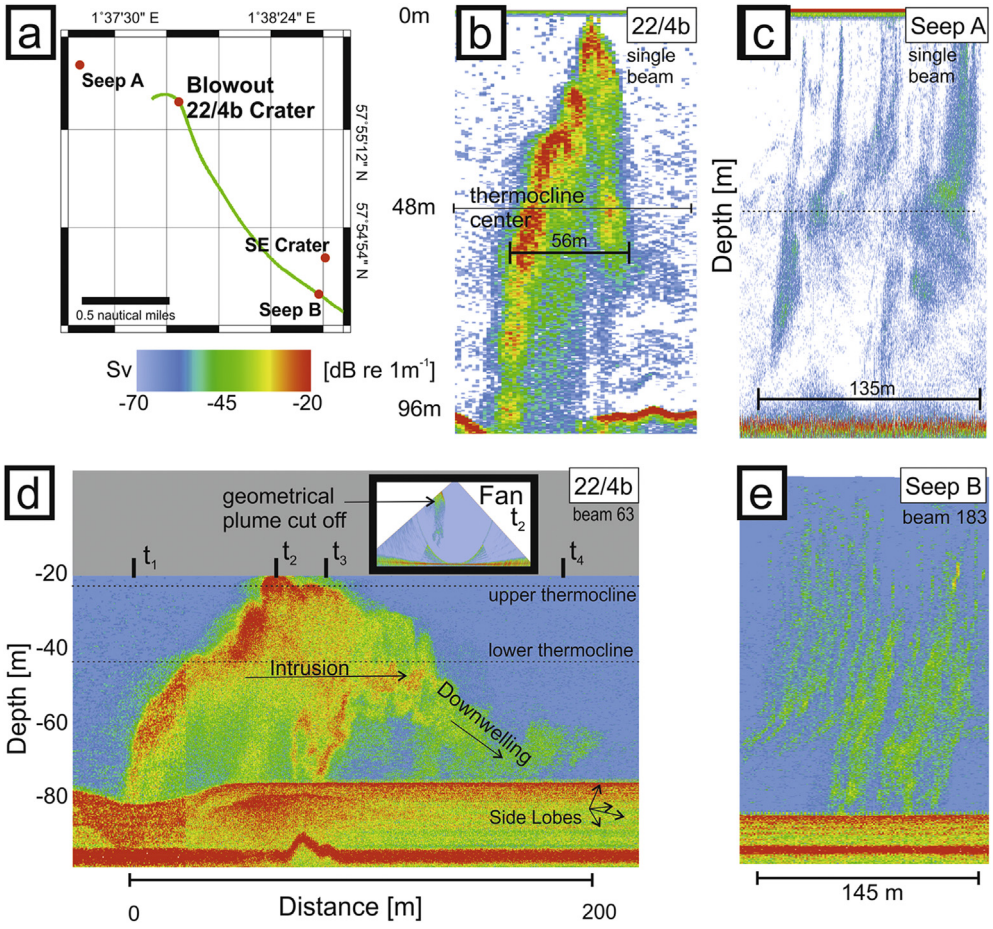

Fig. 8. (a) Cruise track chart with seepage sites (b) single beam echogram recorded in 2006 of the 22/4b seep and (c) showing minor seepage at Seep A (d). Echogram at 22/4b from 2010 representing a slice through the multibeam water column data (beam #63) from the crater towards southeast. Note the top plume loss at t_2 due to geometrical constraints (inlet fan view). (e) Multibeam echogram showing acoustic traces of minor seepage at Seep B. Uniform color code is used in (a) to (e) representing echo volume backscattering strength with increasing intensity from blue, over yellow, to red in dB re 1 m^{-1}. (For interpretation of the references to color in this figure legend, the reader is referred to the web version of this article.)

(Fig. 8b). The highest acoustic volume backscattering Sv values in the calibrated single beam system were found 30 m above the seabed with −19 dB re 1 m^{-1}. Approximately 500 m to the west (1°37′18.03″E; 57°55′23.93″N; Fig. 8a: Seep A) of well site 22/4b, some weaker acoustic bubble backscattering was found over a distance of 135 m reaching −45 dB re 1 m^{-1} (Fig. 8c).

With advances in high resolution water column imaging multibeam sonar, the plume was re-visited in June 2010 with a slightly different thermocline depth. The multibeam survey line runs from NW to SE (Fig. 8a) and elevated acoustic backscattering in the water column data first show up at t_1 right above the 22/4b crater (Fig. 8d). The along-track width of the high intensity plume (red soundings) was up to 22 m, similar to the plume width reported in Schneider von Deimling et al. (2007). The acoustic gas bubble plume extends vertically to the upper thermocline (~20 m) and farther extends laterally at t_2. The topmost part of the plume was lost at this location due to geometrical cut off (Fig. 8d inset). The multibeam image displays a wavy pattern, especially on the upstream (left) and top margin of the acoustic bubble plume, on a meter to dekameter scale. The wavy pattern clearly appears on the lee-side in Supplemental S4, S6, and S9. The multibeam image is similar to single beam observations in Fig. 8b, but has greater spatial resolution. From t_2 until t_4, elevated backscattering values disperse below the thermocline and form an intrusion and downwelling pattern (Fig. 8d). Between t_2 and t_3, a second vertical feature of unknown source is visible between 50 m and 80 m water depth in Fig. 8b. The total width of the plume from t_1 to t_4 was 200 m.

Supplementary video related to this article can be found at http://dx.doi.org/10.1016/j.marpetgeo.2015.07.026.

At 1330 m distance from the crater around the position 1°38′43″ W and 57°54′43″ N, another seep site was identified by its backscatter pattern, i.e. tall and narrow enhanced acoustic scatter originating at the seabed, extending through the water column, and deflected by the currents (Fig. 8e).

4. Discussion

4.1. Ongoing gas discharge at 22/4b

Near-term depletion of gas discharge from the abandoned blowout site 22/4b was postulated more than 20 years ago by former drilling operator Mobil North Sea Ltd. However, based on hydroacoustic (Fig. 8), geochemical (Fig. 6), and visual observations (Fig. 5), a persistent vigorous gas release between 2005 and 2012 is verified by this study. The ongoing high methane discharge activity of well 22/4b maintains the highest known methane surface peak in the open North Sea (Fig. 3) as found more than 10 years earlier (Rehder et al., 1998), and extraordinary dissolved methane concentrations up to 400.000 nM at depth.

Episodic visual observation of the sea surface above well 22/4b over seven years indicate a declining surface bubble diameter area

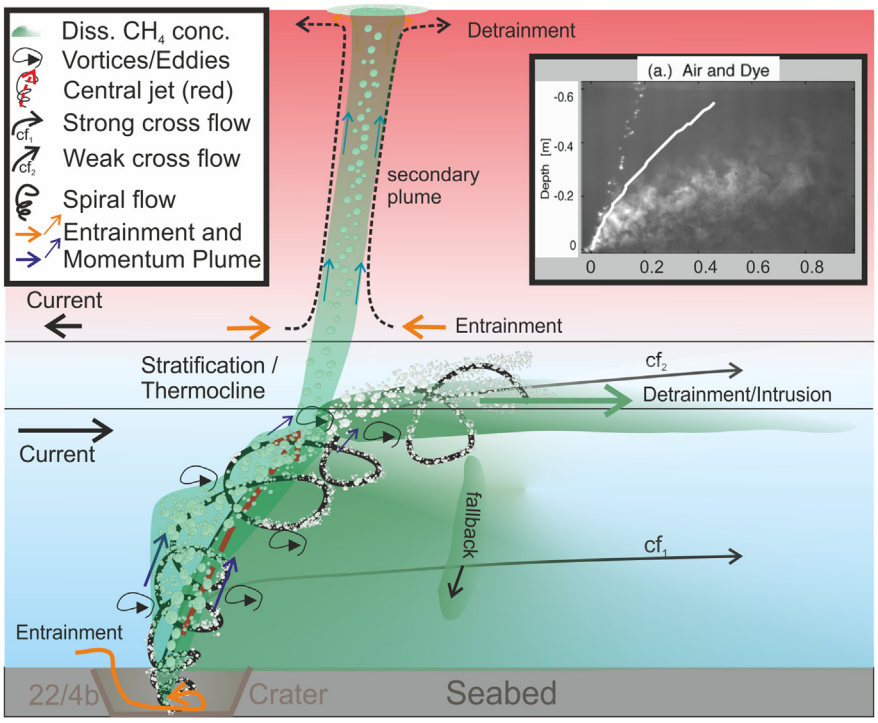

Fig. 9. (a) Schematic sketch indicating mega plume related processes and pathways of gaseous and dissolved methane in response to various cross-flow velocities (Cf_1 and Cf_2, respectively). Inlet shows experimental results about a multiphase air and oil plume in water with distinct separation processes due to cross-flows. Note this laboratory work operates on different scales (1 m range horizontally). Inlet is taken from Socolofsky and Adams (2005) with permission of Prof. Socolofsky.

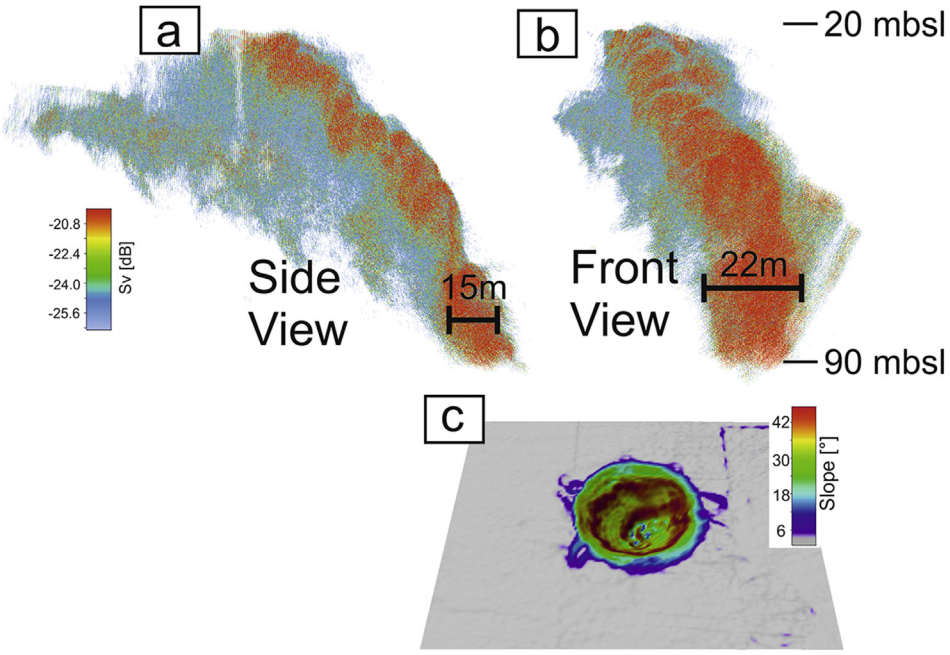

Fig. 10. (a) Extracted water column soundings with high backscatter values plotted in a perspective 3D view. The orientation of the spiral (red) goes towards northwest/up into the field of view (b) 90° degree azimuthal offset presentation (c) Color-coded slope gradient draped onto the bathymetry presented in Fig. 7. Red color indicated a spiral pattern. Note different scaling between the plume and the crater chart. See also supplemental plume video (Supplemental S4). (For interpretation of the references to color in this figure legend, the reader is referred to the web version of this article.)

from about 30 m in 2005 and 2006, to about 15–20 m diameter in June 2010 (Fig. 5a and b; and pers. observation P. Linke, 2006, 2011, 2012; J. Schneider von Deimling in 2005, 2006, 2010). Aircraft-based image analyses revealed a 25 m wide surface plume expression in June 2011 (Gerilowsky et al., in this issue). Although surface bubble plume expressions are influenced by oceanographic parameters and weather conditions, observational snapshots of the bubble plume surface expression between 2005 and 2012 may indicate a decay of blowout activity over the years. This is also supported by much lower surface concentrations measured in 2005 and a smaller lateral extent of elevated surface concentrations compared to 1994 (Rehder et al., 1998).

Currently, discharge of gas and water is still high enough to control distinct morphological features on the seabed with signif-

Table 1
Gas composition of free gas bubbles captured at various depths from the main blowout crater (CE12010_Sta.32, AL290), and from the smaller crater located 1300 m southeast of well 22/4b (CE12010_Sta.41_ROV11).

Station	Depth	CH_4	N_2	O_2	CO_2	Σ C_2..C_6	$\delta^{13}C$–CH_4	Mass balance
	(mbsl)	(ppmv)	(ppmv)	(ppmv)	(ppmv)	(ppmV)	(‰ VPDB)	(%)
CE12010_Sta.32_ROV9	121.5	852,385	55,316	16,558	384	<1	−74.8	92
CE12010_Sta.41_ROV11	106.9	894,514	72,810	20,775	247	<1	−74.9	99
ALK_290_ST_1511_Zodiac_1	0.5	246,808	nm	nm	nm	nm	−71.6	nm
ALK_290_ST_1511_Zodiac_2	0.5	245,783	nm	nm	nm	nm	−71.8	nm
ALK_290_St1529_JAGO	120	886,085	nm	nm	nm	nm	nm	nm

icant changes observed in surface sediment characteristics of the crater center in 2012 (Supplement S10) compared to 2006 (Fig. 4e). The visual observations in 2006 show two sub-basins containing clam shells and barely any soft sediment at the base of the crater (Fig. 4), whereas in 2012, soft sediment covered the clam shells and the two basins (Supplemental S10). Relatively rapid sedimentation and crater infill is expected as observed by Tathje et al. (1999) for a blowout crater in the southern North Sea at 65 m water depth. With an average crater wall slope of 53° in a sandy shallow environment influenced by severe storms and lateral sediment transport, we predict rapid sedimentation infill of the 22/4b crater after the gas release falls below an undetermined threshold. However, until 2012, gas emission with upwelling flow, formation of a new crater (Fig. 5f), and erratic, explosive events (Wiggins et al., in this issue) witness ongoing geological activity at 22/4b and apparently provide transport mechanisms that maintain particle discharge compensating sedimentary infill processes.

4.2. Evidence for low methane transport across the thermocline

Leifer (in this issue) reports 50–142 L s^{-1} in situ gas flux at 12 bar total pressure with a best estimate of 90 L s^{-1} from observations made in 2011 (25 kt CH_4 yr^{-1}). Compared to this value, our 32 L s^{-1} (0.7 kt CH_4 yr^{-1}) sea surface flux estimate from 2006 (see 3.1) represent only 2.7% of the molar in situ CH_4 gas flux at depth, even though strong upwelling flow was observed. Contrary, state-of-the-art modeling suggests much more efficient vertical gas bubble transport and methane fluxes (Leifer et al., in this issue). It has to be noted also that our molar methane surface flux estimate is based on data from 2006 when strong upwelling was observed in the water column, and when surface bubble plume extension exceeded the more recent visual observation of the plume surface expression (yr 2012, Fig. 5b). Thus, the 2.7% (0.7 kt CH_4 yr^{-1}) value given here represents a possible maximum, still lower and therefore in agreement with the threshold detection flux estimate by Gerilowsky et al. (in this issue), who propose surface fluxes less than 5 to 10 kt CH_4 yr^{-1}. Moreover, our 2.7% value corresponds very well with the 3% CH_4 inventory determined in the mixed surface water layer at the blowout in 2011 (Sommer et al., in this issue). The latter was determined by continuous dissolved gas measurements during towed CTD tracks and is related to the total dissolved methane inventory at the blowout site. Sommer et al. (in this issue) could demonstrate that most of the dissolved methane inventory of the blowout remains below the thermocline in June 2011. Our data supported this (measured by discrete hydrocast sampling) resolving dissolved methane concentrations above the thermocline one to two orders of magnitude lower than at depth (Fig. 6a). The concentration in the mixed layer at the background CTD station as well as the bulk (binned median) of the samples gathered immediately above the thermocline, measured close to the blowout, are in the range of 20 nM (Fig. 6a). Although this represents a factor of 7.5 times oversaturation with respect to equilibrium with the atmosphere (C_{equi} at ambient temperature was 2.73 nM) and thus results in a net sea-air flux from the dissolved surface methane pool (i.e. not mediated by direct bubble escape), the gradient across the thermocline considerably limits direct loss from the dissolved methane pool. The seven samples >500 nM above the thermocline (Fig. 6a) could be interpreted by an accidental capturing of bubbles in the Niskin bottles. It is also possible that enhanced concentrations are a result of sampling during a time of very low current velocities (i.e. slack water during tidal change); as discussed later, we suggest that the current-induced separation of the gas plume and the upwelling plume, at this survey location, are a key limit on vertical transport of methane towards the sea surface.

4.3. Acoustic characterization of discharge from well 22/4b

4.3.1. Limits of backscattering strength evaluation

Sonar is very well suited for remote sensing of seep gas bubble scatter due to the large impedance contrast between water and gas, and bubble resonance phenomena (Minnaert, 1933). Therefore, acoustic water column records from 22/4b clearly demonstrate free gas bubble release by enhanced scattering. However, acoustic quantification of gas seep flux is extremely challenging and requires knowledge of depth-specific bubble size distributions to account for the highly non-linear 'backscattering strength' – 'bubble size' relationship (Anderson, 1950), and rise velocities. Moreover, shape variation of gas-filled objects like bubbles (Stanton, 1989), scattering and attenuation from internal structures, and multiple scattering effects (Clay and Medwin, 1977) strongly modulate the backscattering strength. Additionally, non-uniform plume occurrence within the sonar beam complicates discrimination between volume and single target scattering. Given those complications together with uncertainties of bubble rise and upwelling velocities, we consider acoustic inversion of backscattering strength from major or mega plumes into gas flux using the given setup as unrealistic. This is supported by maximum volume backscattering strength at 22/4b measured (up to −18 dB re 1 m^{-1}) at 30 m water depth, which is not in line with the expected maximum fluxes occurring below the thermocline. Moreover, analyses of the backscattering strength over depth variation do not reveal a systematic decay of backscattering strength towards the sea surface. Nevertheless, the volume backscattering strengths at 22/4b of up to −18 *dB* re *1m* $^{-1}$ strongly exceed the ones measured with the same system at the minor natural seep field Tommeliten at similar water depths (Schneider von Deimling et al., 2011). Assuming a linear trend between flux and acoustic backscattering strength after Foote (1983), we consider the very high backscattering strength found at 22/4b measured in 2006 with singlebeam and 2010 with multibeam instrumentation as indicative for mega gas bubble discharge, in concert with video and geochemical records.

4.3.2. Backscattering from the gas bubble plume core

Strongest backscattering values are interpreted to present the well confined inner core of the gas bubble plume (Fig. 8b and d: yellow-red; Supplemental S6, S7, S8 and S9) rising from the crater. The high resolution multibeam data (1.6 m beam resolution at

90 mbsl) demonstrate that individual gas bubble sources, visually identified several meters apart on the seabed (Fig. 4; Leifer, this issue), merge into one acoustic bubble plume farther up in the water column. The interface between the inner core and the ambient water is characterized by a wavy appearance (Fig. 8d, supplemental video S9) in contrast to the interface imaged at minor seep sites (Fig. 8c and e). The formation of these patterns is suggested to be caused by decimeter to meter scale fluid motion eddies observed by video at depth (Supplemental S2, S3). Although not quantifiable, we consider the high resolution imaging of those marginal eddies, possibly for the first time, a potentially very important finding in regard to enhanced turbulence and dissolution processes as suggested in Leifer et al. (in this issue).

4.3.3. Off-plume backscattering features

Weaker scattering outside the inner core of the gas bubble plume broadens towards the current lee-side (Fig. 8b and d, Supplemental Fig. S6). We speculate that small bubbles with <0.5 mm radius (microbubbles) might have been split off the inner core by marginal eddies and are subsequently transported laterally by cross-flow of ambient water. The field data suggest that the majority of the gas bubbles dissolve during their rise. Therefore, the appearance of small bubbles <0.5 mm radius that may behave neutrally buoyant under turbulence, is considered likely in our measurements (resonance radius at 100 m water depth for 70 kHz after Minnaert (1933) is 150 μm). Because turbulence itself is reported a contributor to backscattering at high frequencies (Ross and Lueck, 2003), enclosing much weaker scattering to the luff- and leeside also may be enhanced by turbulence scattering at the interfaces between the inner core of the gas bubble plume, the enclosing momentum plume, and ambient water. An additional explanation for elevated backscatter arises from sediment particle discharge as observed during the JAGO flight (see 3.2) at 22/4b, that would contribute to backscattering, depending mainly on particle size and their number per volume. A future multi frequency measurement could assist discriminating between suggested contributors to enhanced backscattering, i.e. particles, microbubbles, and turbulence.

4.3.4. Upwelling, cross-flow, intrusion, and short-circuiting

Upwelling phenomena were observed by dye tracer injection with JAGO (Fig. 5d) for the initial moments of the plume in the crater with entrainment of ambient water and found to extend into the water column by acoustic Doppler measurements (Wiggins et al., in this issue). When a plume lifts denser water from depth, energy supply and mass replacement are required. Accordingly, a radial water inflow towards the crater was reported from the JAGO dives. We interpret the three crater rim scars (Fig. 7, arrows) as former and recent erosive radial inflow channels cut into the sediment by the suction of water to compensate for mass loss caused by plume upwelling.

During upwelling, continuous dissolution of methane and thus loss of free gas phase lowers the bulk density gradient between the plume and the ambient water. If vertical momentum no longer can lift denser upwelled water against a density gradient (Fig. 6b), the plume will detrain, resulting in the formation of an intrusion layer (Asaeda and Imberger, 1993), as shown by McGinnis et al. (2004) for a stratified freshwater system leading to methane accumulation in this layer. Subsequently, farther rise of gas bubbles may induce a secondary plume above the intrusion layer as described in laboratory experiments (Socolofsky and Rehmann, 2013), likely persisting at 22/4b due to the rise of bubbles up to the sea surface (Figs. 5a,b and 8b). Intrusion at the thermocline occurred at the 22/4b plume as indicated in Fig. 8d and Supplement S6 corresponding to high methane median concentrations (Fig. 6a). The strong methane concentration decrease above 50 m indicates that the methane charged fluid momentum plume only reaches this hydrographic barrier, but does not overcome the strong density gradient at the thermocline (Fig. 6b). However, local breakthrough by upwelling water has been acoustically identified by Wiggins et al. (in this issue), and upwelling up to the sea surface is likely to occur during the unstratified winter time with enhanced methane fluxes to the atmosphere, as predicted for Central and Northern North Sea seep sites (Schneider von Deimling et al., 2011).

If a strong cross-flow bears on an upwelling fluid/gas multiphase plume, the fluid momentum plume may migrate horizontally out of the rising plume (Fig. 9), where trapped bubbles, particles, and turbulence structures maintain acoustic scattering in the displaced water mass imaged in Fig. 8d. This can happen if the lee-side suction force overcomes entrainment flow toward the plume center (Socolofsky and Rehmann, 2013) and heretofore dissolved methane is removed laterally. As a hypothesis, we suggest that the potential cross-flow methane loss may occur as a controlling process in terms of vertical transport efficiency modulated by an hourly tidal timescale. Consequently, we predict maximum vertical transport efficiency of the 22/4b gas plume during the slack water tidal phase.

A downward-orientated pattern is apparent in Fig. 8d in accordance with Wilson et al. (in this issue) and is interpreted as a recirculation of deep, dense upwelled water (Fig. 6b), that migrates toward its neutral buoyancy depth. McGinnis et al. (2004) indicate that such a setting may cause short-circuiting of the plume. The downwelling feature (Fig. 8d) and the path of the dye tracer, which first upwelled from and later returned to JAGO while the submersible remained stationary on the seabed, strongly supports that short-circuiting by a recirculation cell is present at site 22/4b.

4.3.5. Spiral vortex plume

Published models for major subsea gas bubble release sites suggest straight vertical upwelling of gas plumes as a process enhancing seepage-mediated atmospheric methane flux even from greater water depths (Leifer et al., 2006; Solomon et al., 2009). Evaluation of sonar and video data of the 22/4b mega plume gas release draws a different picture. Slow motion video replay of the mega plume released from site 22/4b expose a spiral upward bubble plume motion close to the crater bottom (Supplemental S2). A much broader spiral with increasing diameter, was observed farther up at the crater rim. From video inspection, a high initial rotation velocity at the bottom of the crater is evident. Due to conservation of angular momentum, this spiral vortex is likely to extend farther up into the water column with reduced rotational speed as it broadens. We hypothesize a direct link between the visually recognized rotary motions in the crater and sonar indications of continuing spiral motion farther up in the water column. For verification, high resolution multibeam water column data were filtered for high backscattering values spanning −20 and −26.5 dB to suppress scattering from small bubbles, side-lobe cross-talk, noise, sediment particles, and turbulence scattering. Raypath-corrected data are presented in 3D (Fig. 10, Supplemental S4). Despite the high acoustic scattering of gas bubbles in general, the 70 kHz signals allow for efficient transmission through the bubble cloud, thus permitting not only imaging of the plume envelope as in Schneider von Deimling et al. (2007), but also imaging of its internal structures, like bubble clusters (Supplemental S8). The perspective view on the acoustic plume in Fig. 10 supports observations showing an elliptical spiral extending throughout the water column (Supplemental S4, S9) with minor and major diameter of 10 and 20 m, respectively. 8–10 rotations of the spiral may be estimated from Fig. 10. This corresponds to a circumferential travel path of 400–500 m between the seafloor and sea surface. If bubbles are trapped within the spiral motion, e.g. by strong internal turbulence, their travel time and thus dissolution would be highly enhanced com-

pared to a 90 m vertically upwelled bubble path, especially as turbulence (eddies) may increase gas transfer velocity.

To date, gas bubble driven spiral motions have been observed in engineered plumes in bubble column reactor experiments. Those laboratory experiments were conducted on much smaller scales including wall effects while investigating plume transitions from laminar, to spiral, and to more turbulent (Ulbrecht et al., 1985) modes. Asaeda and Imberger (1993) presented the complexity of engineered bubble plumes of larger scale for environmental applications like lake de-stratification and observed a weak meandering behavior in a gas plume under stratified conditions. Their experiments showed different plume modes controlled by buoyancy frequency, gas flow rate, entrainment coefficient, pressure, and slip velocity as introduced by McDougall (1978). However, the North Sea is characterized by significant ocean currents that might have a very large impact on plume dynamics and fluid motions.

Socolofsky and Adams (2005) discuss the importance of cross-flow strength on plumes. Given the strong tidal control on cross-flow as well as annual build-up and destruction of stratification leading to buoyancy frequency changes in the working area, we accordingly expect complex plume dynamics at site 22/4b with strong modulation of the overall extent on tidal and seasonal time scales.

Most likely, the plume mode has strong implications on the formation of marginal eddies, bubble size evolution and potential bubble fragmentation, effects on dissolution, ambient mixing, bulk vertical rise speed, local detrainment and intrusion, and hold-up times. Therefore, we suggest that the plume mode will strongly affect overall tempo-spatial methane transfer from 22/4b into the water column and atmosphere. We consider an understanding into which mode the plume develops, and how this mode may change due to the cross-flow currents (tides) and seasonal stratification changes, as essential to predict the near and far field methane distribution pattern. Future investigations should consider whether or not spiral evolution of a gas or oil-driven plume might present a typical process. If valid, it further complicates quantitative assessments of gas flux by geochemical or hydroacoustic approaches, but could also provide an explanation for hitherto enigmatic findings at major seep sites, e.g. for the methane peak trapped at depth reported for the Deep Water Horizon Oil Spill (Camilli et al., 2010). However, such very deep gas releases are also strongly controlled by the formation of gas hydrate.

First model attempts accounting for the spiral seep vortex motions described here are presented in Leifer et al. (in this issue). Together with enhanced gas transfer velocity it was found to partly explain the unexpected gas dissolution behavior at 22/4b. Future modeling of 22/4b requires quantitative assessments of spiral plume motions when present. Possibly, this could be realized by future ROV surveys using short range acoustic velocimetry approaches as suggested by Schneider von Deimling and Papenberg (2012).

5. Conclusion

The abandoned well 22/4b, located in the UK North Sea economic zone, is one of the few accessible gas blowout sites in shallow water (~100 m depth) and represents an ideal location to study intense bubble release from the seafloor into the water column and related gas dissolution and plume transport processes. Frequent surveying of near- and farfield blowout site since 2005 characterizes “well 22/4b” to be the most pronounced methane point source in the North Sea. Three mega and dozens of minor and major seeps (first identified at the bottom of the blowout crater in 2006) are mainly releasing methane, formed in shallow sediments by microbial processes. All discovered seeps and an additional major seep found to be active within the crater wall in 2012 demonstrated ongoing gas ebullition until the most recent observations in 2012.

Vigorous gas bubble discharge with upwelling was observed in the blowout crater transporting large quantities of methane bubbles into the water column. However, only a minor fraction of the bubble flux at depth is released into the atmosphere via gas bubble transport, as constrained from visual and hydroacoustic observations. Dissolved methane concentration profiles of the water column support these findings, demonstrating that most emanating gas bubbles efficiently dissolve below the thermocline, although upwelling identified at the seabed may impart a strong uplifting force to the gas plume. However, this massive upwelling was merely found to penetrate the strong thermocline. In contrast, based on acoustic and geochemical data, upwelled waters laterally intruded below the thermocline and partially fall back to the seabed.

Modern high resolution multibeam water column backscatter analyses reveal that one gas plume fed by numerous bubble streams in the crater is rising from depth as an inclined spiral vortex with marginal eddies on a meter scale. The discovered vortex morphology has never been observed at marine gas seeps before, which raises many new questions concerning fluid motion, methane dissolution, and mixing patterns. We expect various plume modes to exist with external controls by tides and annual stratification changes, with a strong overall impact on the fate of methane released from site 22/4b. Mega plumes with observed upwelling do not necessarily give rise to enhanced vertical methane transport through the water column. The existence of strong stratification and/or formation of a spiral vortex potentially linked to enhanced marginal mixing and intrusion, might counteract upwelling mechanisms, but seep investigations performed so far did not account for such complex spiral plume flow.

Acknowledgments

We thank the captain, officers and crew aboard R/V ALKOR, METEOR, and CELTIC EXPLORER especially for their outstanding skills during recovery of heavy gear during rough seas. We gratefully acknowledge the efforts of the JAGO team Karen Hissmann and Jürgen Schauer, the ROV KIEL 6000 team, and thank Maike Nicolai for video editing. We are also grateful for the support of Karen Stange, Andrea Bodenbinder, and Hans Cordt for geochemical analyses at the GC-C-IRMS line and for determination of methane carbon isotopes. The R/V ALKOR cruises were conducted in the framework of the R&D program GEOTECHNOLOGIEN, funded by the German Ministry of Education and Research (BMBF), grant No: 03G0600D and the German Research Foundation (DFG), grant No: 03G0600D. The cruise with R/V CELTIC EXPLORER received funding through the European Community’s 7th Framework Program (FP7/2007–2013) in the EUROFLEETS program and the ECO2 project (grant agreement no. 265847). Data evaluation was performed within the SUGAR II project funded by the BMBF and BMWi (grant 3G819), and in the FUTURE OCEAN project funded by the DFG with grant CP1207.

Appendix A. Supplementary data

Supplementary data related to this article can be found at http://dx.doi.org/10.1016/j.marpetgeo.2015.07.026.

References

Anderson, V.C., 1950. Sound scattering from a fluid sphere. J. Acoust. Soc. Am. 22, 426–431.
Asaeda, T., Imberger, J., 1993. Structure of bubble plumes in linearly stratified environments. J. Fluid Mech. 249 35–35.

Camilli, R., Reddy, C.M., Yoerger, D.R., Van Mooy, B.A., Jakuba, M.V., Kinsey, J.C., Maloney, J.V., 2010. Tracking hydrocarbon plume transport and biodegradation at Deepwater Horizon. Science 330 (6001), 201–204.

Caress, D.W., Chayes, D.N., 2008. Mb-system: Open Source Software for the Processing and Display of Swath Mapping Sonar Data Internet: http://www.mbari.org/data/mbsystem.

Ciais, P., Sabine, C., Bala, G., Bopp, L., Brovkin, V., Canadell, J., Chhabra, A., DeFries, R., Galloway, J., Heimann, M., Jones, C., Le Quéré, C., Myneni, R.B., Piao, S., Thornton, P., 2013. Climate Change 2013: the Physical Science Basis. Contribution of Working Group I to the Fifth Assessment Report of the Intergovernmental Panel on Climate Change. Press, C.U, Cambridge, UK, pp. 465–570.

Clark, J.F., Washburn, L., Emery, K.S., 2010. Variability of gas composition and flux intensity in natural marine hydrocarbon seeps. Geo Mar. Lett. 30 (3–4), 379–388.

Clay, C.S., Medwin, H., 1977. Acoustical Oceanography: Principles and Applications. John Wiley & Sons, New York.

Etiope, G., Klusman, R.W., 2002. Geologic emissions of methane to the atmosphere. Chemosphere 49 (8), 777–789.

Foote, K.G., 1983. Linearity of fisheries acoustics with addition theorems. J. Acoust. Soc. Am. 73, 1932–1940.

Fox, M.A., 1995. Memorandum 22/4b Well Site Hazards. MOBIL North Sea Ltd.

Gerilowski, K., Krings, T., Buchwitz, M., Hartmann, J., Sachs, T., Erzinger, J., Burrows, J.P., Bovensmann, H., 2015. Methane remote sensing constraints on direct sea-air flux from the 22/4b North Sea massive blowout bubble plume. J. Mar. Petrol. Geol. (in this issue).

Hainbucher, D., Pohlmann, T., Backhaus, J., 1987. Transport of conservative passive tracers in the North Sea: first results of a circulation and transport model. Cont. Shelf Res. 7 (10), 1161–1179.

Holt, J., Umlauf, L., 2008. Modelling the tidal mixing fronts and seasonal stratification of the northwest European Continental shelf. Cont. Shelf Res. 28 (7), 887–903.

Hovland, M., Sommerville, J.H., 1985. Characteristics of two natural gas seepages in the North Sea. J. Mar. Pet. Geol. 2 (4), 319–326.

Judd, A.G., Davies, G., Wilson, J., Holmes, R., Baron, G., Bryden, I., 1997. Contributions to atmospheric methane by natural seepages on the UK continental shelf. Mar. Geol. 137 (1), 165–189.

Judd, A.G., 2001. Pockmarks in the UK Sector of the North Sea. UK Department of Trade and Industry (Strategic Environmental Assessment Technical Report).

Judd, A.G., Hovland, M., 2007. Seabed Fluid Flow: the Impact of Geology, Biology and the Marine Environment. Cambridge University Press.

Keir, R.S., Schmale, O., Seifert, R., Sültenfuß, J., 2009. Isotope fractionation and mixing in methane plumes from the Logatchev hydrothermal field. Geochem. Geophys. Geosyst. 10 (5), 1–19.

Kvenvolden, K.A., Lorenson, T.D., Reeburgh, W.S., 2001. Attention turns to naturally occurring methane seepage. Eos, Trans. Am. Geophys. Union 82 (40) 457–457.

Leifer, I., Patro, R.K., 2002. The bubble mechanism for methane transport from the shallow sea bed to the surface: a review and sensitivity study. Cont. Shelf Res. 22 (16), 2409–2428.

Leifer, I., Boles, J., 2005. Measurement of marine hydrocarbon seep flow through fractured rock and unconsolidated sediment. J. Mar. Pet. Geol. 22 (4), 551–568.

Leifer, I., Luyendyk, B.P., Boles, J., Clark, J.F., 2006. Natural marine seepage blowout: contribution to atmospheric methane. Glob. Biogeochem. Cycles 20 (3), 1–9.

Leifer, I., Jeuthe, H., Gjøsund, S.H., Johansen, V., 2009. Engineered and natural marine seep, bubble-driven buoyancy flows. J. Phys. Oceanogr. 39 (12), 3071–3090.

Leifer, I., 2010. Characteristics and scaling of bubble plumes from marine hydrocarbon seepage in the coal oil point seep field. J. Geophys. Res. Oceans (1978–2012) 115 (C11).

Leifer, I., 2015. Seabed bubble flux estimation by calibrated video survey for a large blowout seep in the North Sea. J. Mar. Pet. Geol. (in this issue).

Leifer, I., Judd, A., 2015. The UK22/4b blowout 20 years on: investigations of continuing methane emissions from sub-seabed to the atmosphere in a North sea context. J. Mar. Pet. Geol. (in this issue).

Leifer, I., Solomon, E., Schneider von Deimling, J., Coffin, R., Rehder, G., Linke, P., 2015. The fate of bubbles in a large, intense bubble plume for stratified and unstratified water: numerical simulations of 22/4b expedition field data. J. Mar. Pet. Geol. (in this issue).

McDougall, T.J., 1978. Bubble plumes in stratified environments. J. Fluid Mech. 85 (4), 655–672.

McGinnis, D.F., Lorke, A., Wüest, A., Stöckli, A., Little, J.C., 2004. Interaction between a bubble plume and the near field in a stratified lake. Water Resour. Res. 40 (10).

Milgram, J.H., 1983. Mean flow in round bubble plumes. J. Fluid Mech. 133, 345–376.

Minnaert, M., 1933. On musical air bubbles and the sounds of running water. Philos. Mag. 10, 235–248.

Nauw, J., de Haas, H., Leifer, I., Rehder, G., 2015. A review of oceanographic and meteorologic controls on the fate of North sea methane from a seabed source. J. Mar. Pet. Geol. (in this issue).

Otto, L., Zimmerman, J.T.F., Furnes, G.K., Mork, M., Saetre, R., Becker, G., 1990. Review of the physical oceanography of the North Sea. Neth. J. Sea Res. 26, 161–238.

Pape, T., Bahr, A., Rethemeyer, J., Kessler, J.D., Sahling, H., Hinrichs, K.-U., Klapp, S.A., Reeburgh, W.S., Bohrmann, G., 2010. Molecular and isotopic partitioning of low-molecular-weight hydrocarbons during migration and gas hydrate precipitation in deposits of a high-flux seepage site. Chem. Geol. 269, 350–363.

Rehder, G., Keir, R.S., Suess, E., Pohlmann, T., 1998. The multiple sources and patterns of methane in North sea waters. Aquat. Geochem. 4 (3–4), 403–427.

Rehder, G., Keir, R.S., Suess, E., Rhein, M., 1999. Methane in the northern Atlantic controlled by microbial oxidation and atmospheric history. Geophys. Res. Lett. 26 (5), 587–590.

Rehder, G., Suess, E., 2001. Methane and pCO_2 in the Kuroshio and the South China during maximum summer surface temperatures. Mar. Chem. 75, 89–108.

Ross, T., Lueck, R., 2003. Sound scattering from oceanic turbulence. Geophys. Res. Lett. 30 (6).

Schmale, O., Beaubien, S.E., Rehder, G., Greinert, J., Lombardi, S., 2010. Gas seepage in the Dnepr paleo-delta area (NW-Black Sea) and its regional impact on the water column methane cycle. J. Mar. Sys. 80, 90–100.

Schneider von Deimling, J., Brockhoff, J., Greinert, J., 2007. Flare imaging with multibeam systems: data processing for bubble detection at seeps. Geochem. Geophys. Geosystems 8 (6).

Schneider von Deimling, J., Greinert, J., Chapman, N.R., Rabbel, W., Linke, P., 2010. Acoustic imaging of natural gas seepage in the North Sea: sensing bubbles under control of variable currents. Limnol. Oceanogr. Methods 8, 155–171.

Schneider von Deimling, J., Rehder, G., Greinert, J., McGinnis, D.F., Boetius, A., Linke, P., 2011. Quantification of seep-related methane gas emissions at Tommeliten, North Sea. Cont. Shelf Res. 31 (7), 867–878.

Schneider von Deimling, J., Papenberg, C., 2012. Detection of gas bubble leakage via correlation of water column multibeam images. Ocean Sci. 8 (2), 175–181.

Schroot, B.M., Klaver, G.T., Schüttenhelm, R.T., 2005. Surface and subsurface expressions of gas seepage to the seabed—examples from the southern North Sea. J. Mar. Pet. Geol. 22 (4), 499–515.

Socolofsky, S.A., Adams, E.E., 2005. Role of slip velocity in the behavior of stratified multiphase plumes. J. Hydraul. Eng. 131 (4), 273–282.

Socolofsky, S., Rehmann, 2013. Bubble plumes. In: Fernando, H.J.S. (Ed.). Handbook of Environmental Fluid Mechanics. CRC Press.

Solomon, E.A., Kastner, M., MacDonald, I.R., Leifer, I., 2009. Considerable methane fluxes to the atmosphere from hydrocarbon seeps in the Gulf of Mexico. Nat. Geosci. 2 (8), 561–565.

Sommer, S., Pfannkuche, O., Linke, P., Luff, R., Greinert, J., Drews, M., Gubsch, S., Pieper, M., Poser, M., Viergutz, T., 2006. Efficiency of the benthic filter: biological control of the emission of dissolved methane from sediments containing shallow gas hydrates at Hydrate ridge. Glob. Biogeochem. Cycles 20, GB2019. http://dx.doi.org/10.1029/2004GB002389.

Sommer, S., Schmidt, M., Linke, P., 2015. Continuous inline tracking of dissolved methane plume at a blowout site in the Central North sea UK using a membrane inlet mass spectrometer – water column stratification impedes immediate methane release into the atmosphere. J. Mar. Petrol. Geol. (in this issue).

Stanton, T.K., 1989. Simple approximate formulas for backscattering of sound by spherical and elongated objects. J. Acoust. Soc. Am. 86, 1499–1510.

Thatje, S., Gerdes, D., Rachor, E., 1999. A seafloor crater in the German Bight and its effects on the benthos. Helgol. Mar. Res. 53 (1), 36–44.

Turrell, W.R., Henderson, E.W., Slesser, G., Payne, R., Adams, R.D., 1992. Seasonal changes in the circulation of the northern North Sea. Cont. Shelf Res. 12 (2), 257–286.

Ulbrecht, J.J., Kawase, Y., Auyeung, K.F., 1985. More on mixing of viscous liquids in bubble columns. Chem. Eng. Commun. 35 (1–6), 175–191.

Vielstaedte, L., Karstens, J., Haeckel, M., Schmidt, M., Linke, P., Reimann, S., Liebetrau, V., McGinnis, D.F., Walmann, K., 2015. Quantification of methane emissions at abandoned gas wells in the Central North Sea. J. Mar. Pet. Geol. (This issue).

WASA-Group, 1998. Changing waves and storms in the northeast Atlantic? Bull. Amer. Meteor. Soc. 79, 741–760.

Wiggins, S.M., Leifer, I., Linke, P., Hildebrand, J.A., 2015. Long-term acoustic monitoring at North Sea well site 22/4b. J. Mar. Petrol. Geol. (in this issue).

Wilson, D., Leifer, I., Maillard, E., 2015. Megaplume bubble process visualization by 3D multibeam sonar mapping. J. Mar. Pet. Geol. (in this issue).